Article

Efficient Iron Phosphide Catalyst as a Counter Electrode in Dye-Sensitized Solar Cells

Abdullah Yildiz, Takwa Chouki, Aycan Atli, Moussab Harb, Sammy W. Verbruggen, Rajeshreddy Ninakanti, and Saim Emin*

Cite This: https://doi.org/10.1021/acsaem.1c01628

Read Online

ACCESS | Metrics & More | Article Recommendations | Supporting Information

ABSTRACT: Developing an efficient material as a counter electrode (CE) with excellent catalytic activity, intrinsic stability, and low cost is essential for the commercial application of dye-sensitized solar cells (DSSCs). Transition metal phosphides have been demonstrated as outstanding multifunctional catalysts in a broad range of energy conversion technologies. Here, we exploited different phases of iron phosphide as CEs in DSSCs with an I^-/I_3^--based electrolyte. Solvothermal synthesis using a triphenylphosphine precursor as a phosphorus source allows to grow a Fe_2P phase at 300 °C and a FeP phase at 350 °C. The obtained iron phosphide catalysts were coated on fluorine-doped tin oxide substrates and heat-treated at 450 °C under an inert gas atmosphere. The solar-to-current conversion efficiency of the solar cells assembled with the Fe_2P

material reached $3.96 \pm 0.06\%$, which is comparable to the device assembled with a platinum (Pt) CE. DFT calculations support the experimental observations and explain the fundamental origin behind the improved performance of Fe_2P compared to FeP. These results indicate that the Fe_2P catalyst exhibits excellent performance along with desired stability to be deployed as an efficient Pt-free alternative in DSSCs.

KEYWORDS: iron phosphide, catalyst, counter electrode, dye-sensitized solar cell, solvothermal synthesis
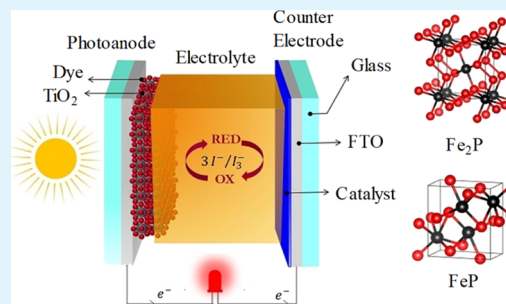
INTRODUCTION

Photovoltaics (PV) is one of the most promising renewable technologies to meet the increasing global energy demands.[1] Dye-sensitized solar cells (DSSCs) with solar-to-electricity conversion efficiency ($\eta \approx 14.2\%$) are considered a favorable alternative to conventional silicon-based solar cells because of the simple assembly technique, stability, mechanical robustness, and the ability to operate at wider angles.[2−4] The outstanding DSSC performance in indoor-light conditions compared to other solar cells makes it a likely candidate for smart PV windows and as a power source for indoor electronic devices. A typical device structure of a DSSC comprises a dye adsorbed on a mesoporous titania photoanode, an electrolyte containing an iodide/triiodide (I^-/I_3^-) redox couple, and a platinum (Pt) counter electrode (CE). Metallic Pt possesses excellent catalytic performance, but the high cost limits its widespread application. A variety of alternative materials has been studied as CE materials for DSSCs, such as carbon-based materials,[5−11] transition metals,[12] metal chalcogenides,[13−15] metal nitrides,[16] metal carbides,[17] polymers,[18] and few compounds made of transition metal phosphides (TMPs).[19−22] Among these materials, TMPs are attractive because they offer good electrical conductivity, catalytic activity, and long-term stability.[23] TMPs with a general formula M_xP_y represent an important class of binary metal/nonmetal catalytic materials with compositions usually being

rich in metal or phosphorus. Owing to their unique functionalities, TMPs were also found to be suitable in electrocatalytic hydrogen evolution reactions,[24,25] oxygen reduction reaction,[26] and oxygen evolution reaction.[27,28] The ability of TMPs to catalyze the reduction of I_3^- makes them promising in DSSCs. Therefore, exploring various TMPs as CE materials for DSSCs is in great demand.

For the first time, we report the use of iron phosphides (FeP and Fe_2P) as CE materials in DSSCs. A simple and cost-effective solvothermal process was used to synthesize iron phosphide catalysts, which were later deposited onto fluorine-doped tin oxide (FTO) substrates. To explain the excellent catalytic activity of Fe_2P for reduction of I_3^-, cyclic voltammetry (CV) and electrochemical impedance spectroscopy (EIS) techniques were employed. DSSCs made of iron phosphides show comparable solar-to-electricity conversion efficiency as Pt CEs. To get relevant information about the fundamental origins behind the better performance of Fe_2P compared to FeP, DFT calculations were performed

A

combining the electronic structure and redox features of the two materials.

■ EXPERIMENTAL SECTION

Preparation of Fe₂P Thin Films. We carried out the synthesis of Fe$_2$P nanoparticles (NPs) under an Ar atmosphere at 300 °C. A typical procedure includes the addition of 11.97 mmol triphenyl-phosphine (TPP, 99%), 3.06 mmol iron pentacarbonyl [Fe(CO)$_5$, 99.99%], 1.0 mL of squalene (SQ, 98%), and 10 mL of oleylamine (OLA, 70%) into a 100 mL three-neck flask. The mixture was heated to 150 °C (ramp rate: 10 °C min^{-1}) and maintained at this temperature until the TPP dissolves. Later, the temperature was gradually increased and held at 300 °C for 15 min. After cooling down the suspension to 60 °C, the Fe$_2$P NPs were isolated by adding a mixture of solvents (ethanol/acetone, v/v 1:1), followed by centrifugation at 8000 rpm for 5 min. The Fe$_2$P NPs were isolated as a solid material after decantation and drying at 50 °C. The powder (0.26 g) thus obtained was suspended in 2 mL of CHCl$_3$ and spin-coated on FTO plates at 1000 rpm for 20 s. The Fe$_2$P catalyst was coated as one layer (Fe$_2$P 1L) and three layers (Fe$_2$P 3L). A similar procedure was also followed during the preparation of the FeP catalyst, with this difference that synthesis was carried out using a mixture of solvents (8 mL of SQ and 3 mL of OLA) at 350 °C for 30 min. The obtained iron phosphide films were heat-treated in a tube furnace at 450 °C for 30 min (heating ramp: 8 °C min^{-1}) under Ar gas (99.999% Messer).

Characterization. The morphologies of the obtained samples were analyzed using a Hitachi SU500 microscope. High resolution (HR) TEM studies were carried out using JEOL 2100F operating at 200 kV. XRD data were recorded with a Miniflex 600 diffractometer (Rigaku), and PDXL software was used for the diffraction analysis (COD database). Rietveld analysis of the iron phosphide phases was carried out using the MAUD program.[29] Transmittance of the CE films was investigated by a UV spectrophotometer (Schimadzu-UV 1700).

Catalyst Evaluation and DSSC Assembly. Cyclic voltammo-grams of I$_3^-$/I$^-$ in acetonitrile were recorded using a three-electrode system where Ag/Ag$^+$ served as the reference electrode, iron phosphide as the working electrode, and a commercial Pt coated (∼1 μm thickness) titanium (Ti) plate (Baoji Qixin Titanium Co., LTD, China) served as the CE. DSSCs with various CEs were assembled following a method given elsewhere.[30] Tafel polarization curves were recorded at a scan rate of 10 mV s^{-1} using symmetrical dummy cells (∼60 μm thick scotch tape). EIS measurements were performed on a Gamry electrochemical workstation (1000E) over the frequency range of 0.05 Hz to 100 kHz at zero bias potential with 10 mV of amplitude in the dark with symmetrical dummy cells. The photocurrent density−voltage characteristics of DSSCs were meas-ured under standard AM 1.5 G illumination (100 mW cm^{-2}) with an active area of 0.25 cm^2 using a solar simulator (ABET, 10500). Stability tests for adhesion were measured by using a four probe measurement station, and for the complete device performance, the tests were conducted under continuous illumination of 10 h.

Computational Details. Based on the Rietveld refined crystal parameters of Fe$_2$P and FeP materials, the predominated (111) exposed facet in Fe$_2$P and (101), (211), and (121) exposed facets in FeP as obtained experimentally for these materials were mainly constructed with respective surface areas of 45.2, 33.4, 63.9, and 51.7 Å^2. All the calculations were carried out in the framework of the spin-polarized periodic DFT by means of the Vienna Ab-Initio Simulation Package (VASP)[31] using the PBE exchange−correlation potential (see Supporting Information).[32] The core electrons were described by the projector-augmented wave (PAW) potentials,[33] and the valence electrons taken into account explicitly in the plane wave descriptions are 3d^{7}4s^1 for Fe and 3s^{2}3p^3 for P. For electron wave function expansion, the highest kinetic energy cutoff between Fe (267.883 eV) and P (270.0 eV) was used. The position of each atom was fully optimized with the conjugate gradient procedure until the residual forces reached values near 10^{-2} eV/Å, and the electronic convergence

for each supercell was near 10^{-5} eV. For sampling the Brillouin zone, the Monkhorst−Pack k-point mesh[34] was set at 5 × 5 × 1 for all the slabs after several tests evaluating the accuracy of the calculations. The spin configuration on each atom was also systematically relaxed at the same time with the electron density distribution during the geometry optimization until reaching the most stable structure, and therefore, the optimal spin magnetic moment was then obtained. The electronic structure calculations were conducted based on the optimized geometries. The analysis covered the orbital contribution of Fe and P in terms of the projected density of states (DOS) on each element. The vacuum energy was acquired from the computed local potential profile going from the bulk to a region away from the surface. To alleviate possible errors in the periodic boundary conditions,[35] dipole corrections perpendicularly to the surface were applied.

■ RESULTS AND DISCUSSION

TEM characterization of the Fe$_2$P powder showed that there are two different populations of NPs in the sample, namely
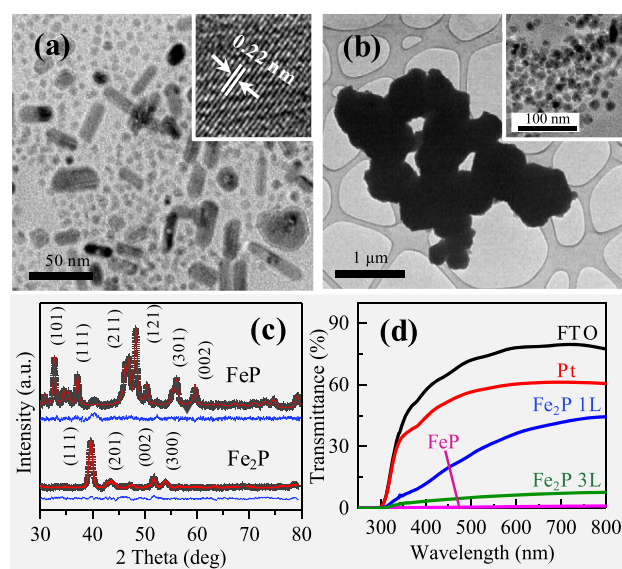

Figure 1. TEM images of (a) Fe$_2$P (inset: HRTEM image) and (b) FeP particles. (c) Refined XRD diffractograms of Fe$_2$P and FeP phases. (d) Transmittance spectra of different CEs.

nanospheres (NSs) and nanorods (NRs) (Figure 1a). The typical sizes of the Fe$_2$P NSs are under 20 nm, whereas those of Fe$_2$P NRs are in the range of 15−50 nm. The HRTEM images show that the lattice spacing equals 0.22 nm, which corresponds to the (111) plane of hexagonal Fe$_2$P (inset of Figure 1a). In the case of the FeP sample, the individual particles are agglomerated into larger aggregates such as microspheres with typical sizes ranging from 400 to 1200 nm (Figure 1b). The inset of (b) shows individual FeP nanoparticles which form each microsphere. The sizes of these NPs are under 20 nm.

The diffraction patterns of iron phosphides are assigned to different phases: hexagonal for Fe$_2$P (P62m, PDF# 1008826) and orthorhombic for FeP (Pbnm, PDF# 9008932) (Figure 1c). The Rietveld refined crystal parameters for these phases are a = b = 5.851 ± 0.0034 Å and c = 3.507 ± 0.0026 Å for Fe$_2$P and a = 3.101 ± 0.0003 Å, b = 5.195 ± 0.0006 Å, and c = 5.791 ± 0.0007 Å for FeP. These values are in good agreement with the literature[36] and calculated DFT lattice parameters (a = b = 5.79 Å and c = 3.41 Å for Fe$_2$P and a = 3.03 Å, b = 5.14 Å, and c = 5.75 Å for FeP).
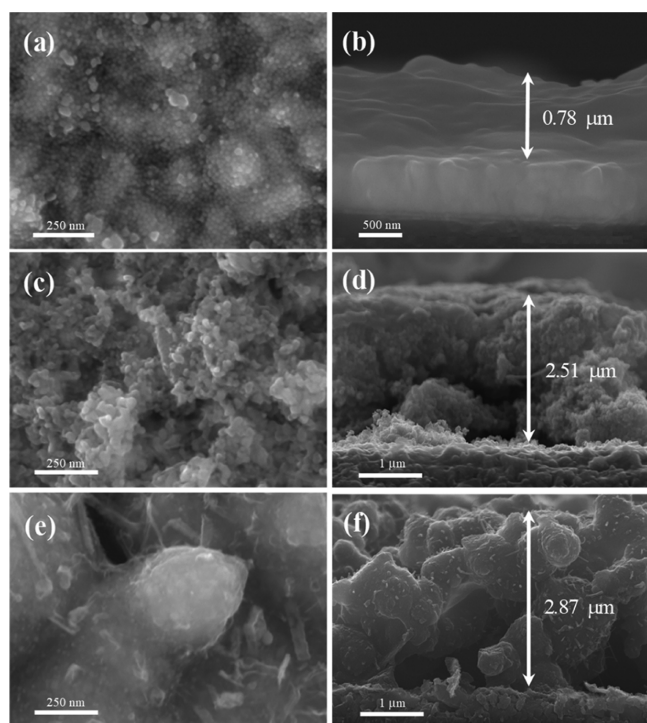
Figure 2. SEM images of CEs. Top (left) and cross-sectional (right) views of (a,b) Fe_2P 1L, (c,d) Fe_2P 3L, and (e,f) FeP.
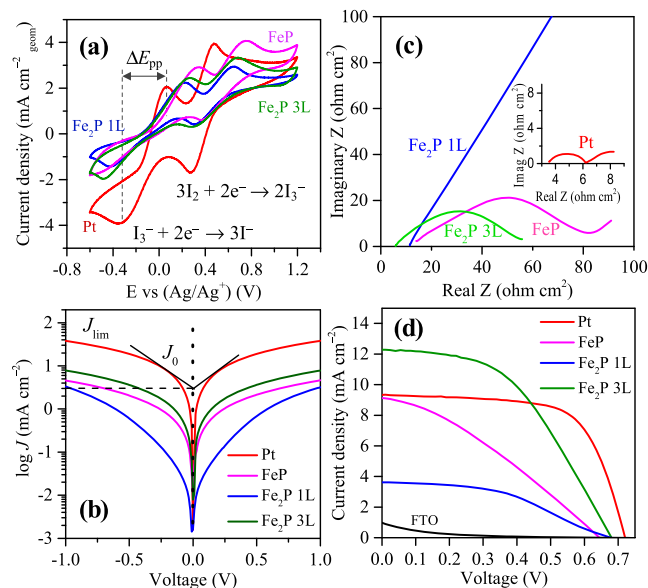
Figure 3. (a) Cyclic voltammograms recorded at 50 mV s^{-1} using different CEs. (b) Tafel plots. (c) Nyquist plots of EIS for the symmetrical cells fabricated with two identical electrodes in the I_3^-/I^- electrolyte system. (d) $J-V$ curves of the devices assembled with different CEs.

The crystallite size and the intrinsic strain calculated using the Williamson–Hall method yielded, respectively, an average size of 18 ± 0.0010 nm and $4.5 \times 10^{-3} \pm 0.0007$ a.u. for Fe_2P and 21 ± 0.0136 nm and $3.3 \times 10^{-3} \pm 0.0091$ a.u. for FeP (Figure S1). The reliability of the refinement was assessed by the low values of the weighted profile (R_{wp}) factor; the values are $R_{wp} = 4.23\%$ for Fe_2P and $R_{wp} = 3.20\%$ for FeP. The

Table 1. Electrochemical Parameters Extracted from the CV, Tafel, and EIS (Symmetric CEs) Plots

devices	Pt	Fe_2P 1L	Fe_2P 3L	FeP
ΔE_{pp} (mV)	387	636	719	823
J_{pc} (mA cm^{-2})	3.91	1.44	1.96	1.55
J_0 (mA cm^{-2})	17.61	0.27	2.82	1.48
J_{lim} (mA cm^{-2})	38.03	3.33	7.87	4.59
R_s (Ω cm^2)	3.48	11.29	5.75	13.34
R_{ct} (Ω cm^2)	2.33	73.52	52.01	71.15

processed data meet the established criteria ($R_{wp} < 20\%$) for good refinement.[37]

Characterization of iron phosphides was also carried out using Raman studies (Figure S2). The appearance of two prominent peaks at 1321 and 1583 cm^{-1} in the Raman spectra is assigned to the G (associated with the tangential stretching mode) and D (arising from the disordered hybridization carbon) bands of the graphitic structure, respectively.[38] Carbon is formed after heat treatment at elevated temperatures under an inert atmosphere. The source of this carbon is the capping molecules on the surface of iron phosphide particles that pyrolyze to graphitic carbon after thermal treatment. The characteristic Raman signature peaks of Fe_2P appear at 164, 187, and 205 cm^{-1} and those of the FeP phase at 194, 211, 254, 296, and 303 cm^{-1}. These results coincide with the reported Raman shifts for Fe_2P and FeP phases.[39,40]

The obtained iron phosphide particles were dispersed in $CHCl_3$ and coated onto FTO substrates to use them as CE catalysts in DSSCs. The transmittance spectra of FeP, Fe_2P, and Pt coated FTO films are shown in Figure 1d. By increasing the film thickness of Fe_2P, the transmittance gradually drops. A thicker film with a low transmittance can be beneficial for the back reflection of the incident light in the DSSC device.[41] In particular, it can contribute to the enhancement of short-circuit current density (J_{sc}).

The morphology and thickness of the thermally treated CEs were studied using SEM, as shown in Figure 2. In the Fe_2P 1L sample, the film is composed of evenly coated NPs that are arranged in a porous network with a thickness of 0.78 μm. Similar morphology with a porous structure was also found for the Fe_2P 3L sample. The thickness of the Fe_2P 3L film is 2.51 μm. It is evident that a drastic change in transmittance of Fe_2P 3L occurs due to the film thickness. This film is completely nontransparent. The surface area and pore size distributions of the Fe_2P sample (in the powder form) were analyzed by N_2 adsorption–desorption isotherms (Figure S3).[42] The BET surface area was found to be 13.97 m^2 g^{-1}, and the measured Barrett–Joyner–Halenda (BJH) median pore diameter was 22.64 nm with a pore volume of 0.052 cm^3 g^{-1}. In the case of the FeP sample that is composed of microspheres, the BET surface area was determined to be 32.11 m^2 g^{-1}, the BJH adsorption median pore diameter was 11.01 nm, and the pore volume was 0.087 cm^3 g^{-1} (Figure S3). As observed earlier in the TEM images, each FeP microsphere consists of many NPs. Because of this reason, it seems that the FeP sample exhibits a higher surface area in comparison to Fe_2P. EDX analysis revealed that the atomic composition of the elements in the FeP film corresponds to 1:1 for Fe and P (Figure S4). The thicknesses of the resulting FeP films, as determined from cross-sectional SEM images, are equal to 2.87 μm (Figure 2f). The thicknesses of the Fe_2P 3L and FeP films are thus very similar, providing a fair basis for comparison.

Table 2. EIS and PV Parameters of the Complete DSSC Devices Assembled with Different CEs

| device	J_{sc} (mA cm^{-2})	V_{oc} (V)	FF	η (%)	R_1 (Ω cm^2)	R_2 (Ω cm^2)	R_s (Ω cm^2)	R_{CE} (Ω cm^2)	R_{tr} (Ω cm^2)	f_{max} (Hz)	$\tau_{e\ Bode}$ (ms)
Fe$_2$P 1L	3.63	0.68	0.43	1.07	172.89	1678.74	51.02	7.23	1855.04	31.2	5.1
FeP	9.14	0.64	0.33	1.91	192.51	291.88	55.92	43.27	247.51	113.2	1.4
Fe$_2$P 3L	12.3	0.69	0.47	3.96	84.39	925.60	24.78	43.02	355.60	29.8	5.3
Pt	9.32	0.71	0.67	4.47	19.91	2182.65	5.73	50.61	213.40	15.6	10.2
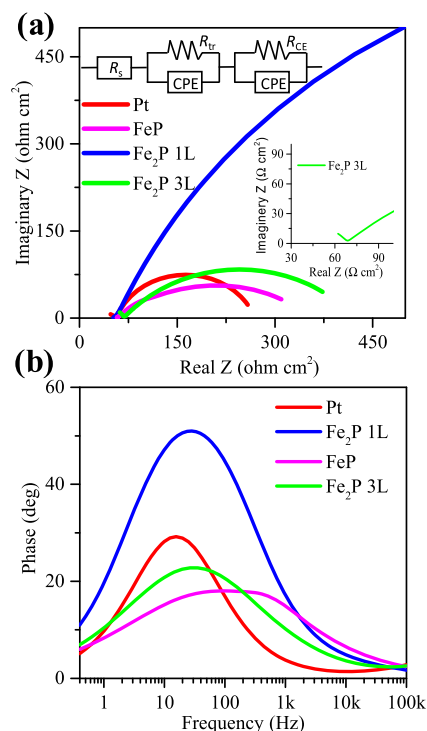
Figure 4. (a) Nyquist and (b) Bode impedance plots of complete DSSC devices with different CEs recorded in the dark under open-circuit potentials. The inset of (a) is the equivalent circuit used to model the EIS data.
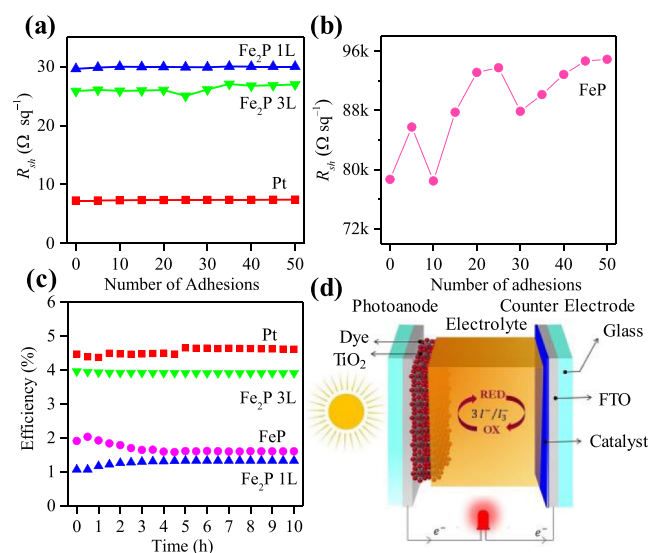
Figure 5. (a,b) Sheet resistance of different CEs vs adhesion cycles. (c) Power conversion efficiency vs time. (d) Scheme of a DSSC.

To examine the catalytic activities of iron phosphide CEs, CV studies were carried out in a three-electrode system (working electrode, reference electrode, and CE). The
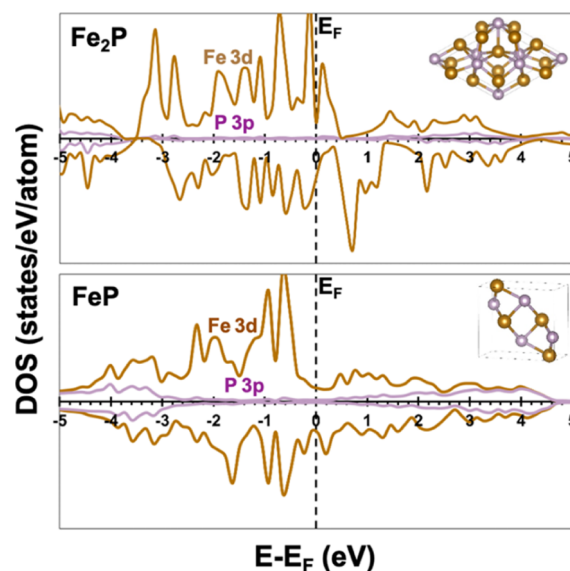

Figure 6. DFT-based computed electronic DOS of bulk Fe$_2$P and FeP materials with spin-up and spin-down states. Their corresponding unit cell crystal lattice is also shown. The projected DOS is shown in brown for Fe and purple for P.

electrolyte used was acetonitrile containing 10 mM NaI, 1 mM I$_2$, and 0.1 M NaClO$_4$. The positive current peaks in the cyclic voltammogram correspond to the oxidation reaction, and the negative current peaks to the reduction reaction (Figure 3a).

The left pair of peaks (>0.2 V vs Ag/Ag$^+$) represents the redox reaction I$_3^-$ + 2e$^-$ ↔ 3I$^-$. On the other side, the right pair is for the redox reaction 3I$_2$ + 2e$^-$ ↔ 2I$_3^-$ (Figure 3a). CE catalytic ability is estimated by two characteristic parameters, peak current density (J_{pc}) and peak-to-peak separation (ΔE_{pp}). The values of ΔE_{pp} are calculated from $\Delta E_{pp} = E_p(\text{anodic}) - E_p(\text{cathodic})$. ΔE_{pp} follows an order of FeP > Fe$_2$P 3L > Fe$_2$P 1L > Pt (Table 1). The lower values of ΔE_{pp} indicate the smaller overpotential of the reduction reaction. Even though Fe$_2$P 1L follows Pt, it suffers from a low current density, rending its PV performance poor. However, Fe$_2$P 3L is superior to FeP in catalyzing the reduction of I$_3^-$ to I$^-$.

In DSSCs, a CE is responsible to collect electrons from the external circuit and for regeneration of the I$_3^-$ ions in the electrolyte. The higher cathodic peak current density (J_{pc}) indicates the better electrocatalytic activity of the CE in DSSCs. The J_{pc} values of the four tested CEs follow the order of Pt > Fe$_2$P 3L > Fe$_2$P 1L > FeP (Table 1). These results demonstrate that Fe$_2$P is again better than FeP as the CE material.

To further ascertain the electrocatalytic activity of CEs, exchange current density (J_0) and limiting current density (J_{lim}) of the reduction process are determined from the Tafel polarization curves measured in symmetrical dummy cells (Figure 3b). The intersection of the cathode branch and the
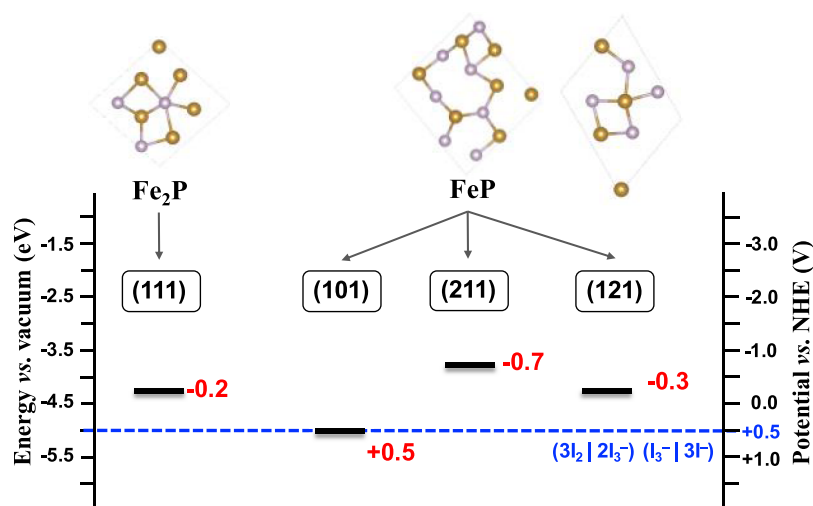
Figure 7. DFT-based computed Fermi energy positions for the optimized (111)-oriented Fe_2P slab and for the optimized (101)-, (121)-, and (211)-oriented FeP slabs relative to vacuum and the NHE. The top view depiction of the (111), (101), and (121) surface atomic composition is shown.

equilibrium potential line in the Tafel zone correspond to the value of J_0. Here, J_0 signifies how fast the electron transfer process occurs on the CE/electrolyte interface. The value of J_0 is inversely proportional to the charge transfer resistance (R_{ct}).[43] Diffusion characteristics of I_3^- are associated with J_{lim} corresponding to the saturated current value in the Tafel polarization curve.

Its value can be estimated from the cathodic branch intercept on the ordinate in the diffusion zone. A higher value of J_{lim} implies a larger value of the electrolyte ion diffusion rate in the CE.[44] Therefore, higher values of J_0 and J_{lim} account for the superior catalytic activity of CEs. The values of J_0 and J_{lim} increase in the following order: Fe_2P 1L < FeP < Fe_2P 3L < Pt (Table 1). The lower values of J_{lim} in iron phosphides can be associated with the microstructure of the CE providing the contact with FTO and the diffusion of the I^-/I_3^- electrolyte in the porous matrix. A nonflat and porous surface of the Fe_2P CE might lead to a reduction in the J_{lim} value compared to that of the Pt CE.[45] Although the J_{lim} value of iron phosphide is lower, these results unambiguously reveal that the Fe_2P 3L electrode offers a promising catalytic activity toward I_3^- reduction and presents a low-cost alternative to Pt.

Interfacial charge-transfer kinetics on the CEs are analyzed using EIS measurements. Figure 3c depicts Nyquist plots of symmetric CEs (CE/electrolyte/CE). The Randels-type equivalent circuit (Figure S5) is utilized to fit EIS curves, and fitting parameters are listed in Table 1. The equivalent circuit includes a series resistance (R_s) associated with the sheet resistance of FTO and resistance of the electrolyte, a charge transfer resistance (R_{ct}) representing the electrocatalysis activity at the CE/electrolyte interface, and a constant phase element (CPE). The R_s values of the four tested CEs follow the order FeP > Fe_2P 1L > Fe_2P 3L > Pt (Table 1). A relatively low value of R_s[46] for Fe_2P 3L demonstrates that good quality adhesion and contact occur between the Fe_2P film and FTO. Furthermore, it is known that a higher R_s value negatively affects the fill factor (FF) of a DSSC. Apart from that, a consistent trend is observed between the value of R_{ct} and J_0.

The highest J_0 value can be ascribed to the lowest R_{ct} value. Even though the R_{ct} value of the tested CEs is greater than that of Pt, these values are comparable with those reported

previously.[46] R_{ct} is considered a crucial parameter in evaluating the intrinsic electrocatalytic activity of a CE, and the lower R_{ct} value generally represents the higher electrocatalytic activity toward triiodide reduction.[19] The low R_s and R_{ct} values recorded for the Fe_2P 3L sample can be attributed to its superior electrocatalytic activity and conductivity. The Bode plots of the dummy cell based on two identical and symmetrical CEs are shown in Figure S5. The lifetimes of electrons participating in the I_3^- reduction reaction are related to the peak frequency in the Bode spectrum (Figure S5). The higher the peak frequency, the shorter the electron lifetime, indicating the higher catalytic activity of the material for the reduction of I_3^-. The results indicate that Pt has the fastest electron transfer rate at the CE/electrolyte interface, followed by FeP and Fe_2P 3L. The higher peak frequency of FeP with respect to Fe_2P 3L is an opposite trend with the calculated R_{ct} values. The observed lower peak frequency in Fe_2P 3L could be associated with the diffusion impedance, which is a 100,000-fold higher than in FeP (Table S1). Although the pore diameters estimated using N_2 physisorption studies in the Fe_2P powder are larger than those in the Fe_2P powder, the situation might be different in the case of the thin film. This result confirms that the lower diffusion resistance in the FeP electrode has an advantage over the Fe_2P 3L electrode for fast mass transport. However, the lower R_{ct} values of Fe_2P 3L make it more attractive as the CE for DSSCs. Furthermore, these iron phosphide films still need optimization in terms of porosity and thickness for best device performance.

The measured photocurrent density−voltage curves (J−V) of the devices based on different CEs are shown in Figure 3D. The detailed PV parameters of the devices, including J_{sc}, open-circuit voltage (V_{oc}), FF, and solar-to-electricity conversion efficiency (η), are listed in Table 2. The device with bare FTO shows poor overall η of 0.05 ± 0.01%. After coating the iron phosphides onto FTO, the η value of the devices is significantly enhanced. In the device assembled with Fe_2P 3L, η reaches 3.96 ± 0.06% with a J_{sc} of 12.3 ± 0.07 mA cm^{-2}, a V_{oc} of 0.69 ± 0.02 V, and a FF of 0.47. The power conversion values are quite close to the DSSC that incorporates the Pt CE (4.47%). The excellent efficiency of Fe_2P 3L is primarily due to the high J_{sc} value (Table 2). It is noteworthy that the J_{sc} value of the

device assembled with the Fe$_2$P 3L CE is greater than that of the Pt CE. Because the devices are assembled with the same photoanode and electrolyte, the observed variations in solar cell parameters are solely attributed to a change in the CE. An increase in J_{sc} and FF values can be mainly associated with the better electrocatalytic ability of a CE and a fast charge migration at the CE/electrolyte interface in the devices. The proposed CEs made of iron phosphides suffer from low FF values presumably originating from the low conductivity of FeP and Fe$_2$P compared to a Pt film. The FF values of DSSCs based on Fe$_2$P are smaller than those for Pt and can be attributed to different parameters like the higher R_{ct} value, shunt resistance, lower conductivity, diffusion related resistances, or weak contact between the iron phosphide and the FTO substrate.

To address the fluctuations in FF values, we analyzed the $J-V$ curves. From the slope of V_{oc}, the series resistance (denoted by R_1) was estimated, and from J_{sc} points, the shunt resistance (denoted by R_2) was determined. For a high-performing DSSC device, low R_1 value and high R_2 value are expected. Therefore, FF can be parametrized by aiming for a smart and easy comparison with the ratio of shunt and series resistances (R_2/R_1). The value of this ratio was calculated as 9.71, 1.52, 10.97, and 109.63 for the Fe$_2$P 1L-, FeP-, Fe$_2$P 3L-, and Pt-based device, respectively. Furthermore, these calculated values follow the trend in the FF of DSSCs, which are 0.43 for Fe$_2$P 1L, 0.33 for FeP, 0.47 for Fe$_2$P 3L, and 0.67 for Pt.

To gain a deeper understanding of different resistances and electron lifetimes (τ_e), EIS of complete DSSC devices was measured. In a typical Nyquist plot, there is a small semicircle in the high-frequency range and a large semicircle in the low-frequency range (Figure 4a). The small semicircle is correlated to the resistance of the electrolyte/Pt CE interface (R_{CE}), and the larger semicircle is associated with the charge transfer resistance (R_{tr}) at the TiO$_2$/electrolyte interface.[47] The R_{tr} values give a clear idea of the recombination behavior of electrons through the semiconductor oxide layer. Lower R_{tr} values mean better performing DSSC devices. Another parameter that is associated with the recombinations is τ_e. This parameter is inversely proportional to the maximum frequency (f_{max}) and can be extracted from the Bode plot (Figure 4b).[47] f_{max} in the large semicircle region relates to τ_e with the following equation: $\tau_e = 1/2\pi f_{max}$ (Table 2). The Fe$_2$P 3L-based DSSCs demonstrate a higher τ_e value compared to FeP and Fe$_2$P 1L, which accounts for the uninterrupted electron transport through the TiO$_2$ layer to a longer distance, leading to the enhanced η value.

In early reports on iron phosphides, it was demonstrated that phosphorus can enhance the electrical resistivity of iron.[48] The resistivity of iron phosphides decreases with the decreasing phosphorus content. In addition to intrinsic conductivity, other factors that can contribute to the overall η efficiency of iron phosphide films are the catalytic activity, surface area, and optical transmittance. A comparison of the calculated electrochemical active surface area (ECSA) determined from EIS studies shows that the films exhibit a difference in surface areas (Figure S6).

The ECSA of the iron phosphide films follows the order: 20.5 cm^2 for Fe$_2$P 3L, 14.9 cm^2 for FeP, and 4.7 cm^2 for Fe$_2$P 1L. It is obvious that a higher surface area is beneficial for the excellent performance of the Fe$_2$P 3L thin film. Nevertheless, the ECSA is not the only parameter that affects the overall performance of the CEs, and other parameters are equally important. For example, the opaque nature of Fe$_2$P 3L in comparison to Fe$_2$P 1L is advantageous for declining the loss of the incident light on account of its lower transmittance that can induce light scattering and favorably influence the value of J_{sc}.[49] The catalytic activity of the Fe$_2$P 3L CE is better than that of the FeP CE. On the other hand, the J_{sc} value of the DSSC device assembled with the Fe$_2$P 1L CE is worst due to its poor catalytic activity and relatively higher transparency. Ultimately, the achieved overall performance of the device assembled with the Fe$_2$P 3L CE reaches ≈89% of the device assembled with a standard Pt CE.

Mechanical stability of the different CEs was studied by rolling a 2 kg disk under 3 M removable tape (Figure 5a,b).[50] The tape is removed at a 90° angle after disk rolling. To trace the surface adhesion features of the CEs, the fluctuation in the sheet resistance (R_{sh}) is measured. The order of R_{sh} is Pt (7.28 Ω sq^{-1}) < Fe$_2$P 3L (25.82 Ω sq^{-1}) < Fe$_2$P 1L (29.61 Ω sq^{-1}) < FeP (78 kΩ sq^{-1}). A lower R_{sh} value of Fe$_2$P 3L may be ascribed to its vigorous adhesion to FTO.[41] The change in R_{sh} is less than 1%, demonstrating the excellent mechanical adhesion of Fe$_2$P 3L deposited on the FTO substrate. The stability of the CEs was also studied in the DSSC configuration (Figure 5c). The long-term stability tests show that Pt and Fe$_2$P 3L CE-based devices perform comparably under simulated solar light illumination (AM1.5G). Both Pt and Fe$_2$P 3L CE-based devices retain their original efficiency value over the 10 h testing period. In contrast, a slight decrease in activity is observed in the case of the FeP CE-based device (Figure 5c).

Figure 6 shows the computed electronic structures of bulk Fe$_2$P and FeP materials with spin-up and spin-down states, highlighting their magnetic behavior. It can be clearly observed in both cases that the electronic states near the Fermi level, which are directly involved in the catalysis, are mainly made by Fe 3d orbitals. In both cases, the contribution of P 3p orbitals is negligible near the Fermi level. They appear much deeper in the energy scale. This result indicates that Fe is mainly involved in the catalytic processes. Note that the spin-up Fe 3d orbital density near the Fermi level is higher in Fe$_2$P than in FeP, and this is expected to exert an impact on the catalytic performance results. Additional magnetization calculations also confirmed the higher magnetic nature in Fe$_2$P with respect to FeP with obtained magnetic moments of 4.8 μ_B and 1.5 μ_B, respectively, essentially originating from the Fe atoms.

Figure 7 shows the DFT-based computed Fermi energy positions for the optimized (111)-oriented Fe$_2$P slab and for the optimized (101)-, (121)-, and (211)-oriented FeP slabs relative to vacuum and the normal hydrogen electrode (NHE). It can be observed that the (111) surface of Fe$_2$P together with the (211) and (121) surfaces of FeP are suitable candidates for the iodine reduction reaction, while the (101) surface of FeP is not suitable. Note that the standard reduction potential of I$_3^-$ + 2e$^-$ → 3I$^-$ is located at 0.536 V versus NHE (Figure 7). Moreover, the top view depiction of (111) in Fe$_2$P and (101) and (121) in FeP surfaces reveals that the surface atomic Fe/P ratio is 2:1 for (111) in Fe$_2$P, while it is 1:1 for (211) and (121) in FeP (Figure 7). It must be noted that the (111) crystallographic plane is the only major orientation in the case of Fe$_2$P, while (101), (211), and (121) are the major crystallographic planes in FeP (Figure 1c). Consequently, the percentage of the (111) facets exposed on Fe$_2$P is expected to be much higher than those of (101), (211), and (121) facets exposed on FeP.

Overall, when the electronic structure and redox features are compared between the two Fe$_2$P and FeP materials, we can clearly observe a higher Fe 3d orbital density near the Fermi level in Fe$_2$P. Moreover, according to XRD patterns, the percentage of the active and only major (111) surface of Fe$_2$P is much higher with respect to the (211) and (121) surfaces of FeP. By combining all these results, we can explain the fundamental origin behind the better catalytic performance of Fe$_2$P compared to FeP.

■ CONCLUSIONS

The study presents low-cost iron phosphide catalysts and their utilization as CEs in DSSC studies. In particular, DSSCs assembled with FeP and Fe$_2$P CEs were successfully demonstrated. The devices assembled with Fe$_2$P 3L CEs outperformed those constructed with FeP CEs. The J_{sc} value of the PV device based on Fe$_2$P 3L (12.3 ± 0.07 mA cm^{-2}) was larger than that of the conventional Pt (9.32 ± 0.04 mA cm^{-2}) CE. The overall power conversion performance of the device assembled with the Fe$_2$P 3L CE ($3.96 \pm 0.06\%$) was comparable to that of the device assembled with the Pt CE. The outstanding catalytic activity of Fe$_2$P 3L, as determined using EIS, shows a lower R_{ct} value (≈ 52 Ω cm^2) with respect to the FeP CE. DFT calculations supported the experimental observations and explained the fundamental origins behind the better performance of Fe$_2$P compared to FeP. This study promotes the use of iron phosphide catalysts made of earth-abundant elements as efficient Pt-free alternatives in DSSCs.

■ ASSOCIATED CONTENT

ⓈI Supporting Information

The Supporting Information is available free of charge at https://pubs.acs.org/doi/10.1021/acsaem.1c01628.

Rietveld refinement analysis, Williamson−Hall method, SEM image of the FeP film with EDX, DFT experimental section, physisorption measurements, and Bode and Nyquist plots (PDF)

■ AUTHOR INFORMATION

Corresponding Author

Saim Emin − *Materials Research Laboratory, University of Nova Gorica, 5270 Ajdovščina, Slovenia;* ⓞ orcid.org/0000-0003-1918-3997; Phone: +38630264591; Email: saim.emin@ung.si

Authors

Abdullah Yildiz − *Department of Energy Systems Engineering, Faculty of Engineering and Natural Sciences, Ankara Yıldırım Beyazıt University, 06010 Ankara, Turkey*

Takwa Chouki − *Materials Research Laboratory, University of Nova Gorica, 5270 Ajdovščina, Slovenia*

Aycan Atli − *Department of Energy Systems Engineering, Faculty of Engineering and Natural Sciences, Ankara Yıldırım Beyazıt University, 06010 Ankara, Turkey;* ⓞ orcid.org/0000-0003-1328-8042

Moussab Harb − *KAUST Catalysis Center (KCC), Physical Sciences and Engineering Division (PSE), King Abdullah University of Science and Technology (KAUST), 23955-6900 Thuwal, Saudi Arabia;* ⓞ orcid.org/0000-0001-5540-9792

Sammy W. Verbruggen − *Sustainable Energy, Air & Water Technology (DuEL), Department of Bioscience Engineering and NANOlab Center of Excellence, University of Antwerp, 2020 Antwerp, Belgium;* ⓞ orcid.org/0000-0003-2372-9630

Rajeshreddy Ninakanti − *Sustainable Energy, Air & Water Technology (DuEL), Department of Bioscience Engineering and NANOlab Center of Excellence, University of Antwerp, 2020 Antwerp, Belgium; Electron Microscopy for Material Science (EMAT), Department of Physics, University of Antwerp, 2020 Antwerp, Belgium*

Complete contact information is available at:
https://pubs.acs.org/10.1021/acsaem.1c01628

Author Contributions

A.Y. and S.E. contributed equally to this work. The manuscript was written through the contributions of all authors. All authors have given approval to the final version of the manuscript.

Notes

The authors declare no competing financial interest.

■ REFERENCES

(1) Meyer, G. J. Chemist's Quest for Inexpensive, Efficient, and Stable Photovoltaics. *J. Phys. Chem. Lett.* **2011**, *2*, 1965−1966.

(2) Misra, R.; Maragani, R.; Arora, D.; Sharma, A.; Sharma, G. D. Positional isomers of pyridine linked triphenylamine-based donor-acceptor organic dyes for efficient dye-sensitized solar cells. *Dyes Pigm.* **2016**, *126*, 38−45.

(3) Islam, A.; Akhtaruzzaman, M.; Chowdhury, T. H.; Qin, C.; Han, L.; Bedja, I. M.; Stalder, R.; Schanze, K. S.; Reynolds, J. R. Enhanced Photovoltaic Performances of Dye-Sensitized Solar Cells by Co-Sensitization of Benzothiadiazole and Squaraine-Based Dyes. *ACS Appl. Mater. Interfaces* **2016**, *8*, 4616−4623.

(4) Han, L.; Islam, A.; Chen, H.; Malapaka, C.; Chiranjeevi, B.; Zhang, S.; Yang, X.; Yanagida, M. High-efficiency dye-sensitized solar cell with a novel co-adsorbent. *Energy Environ. Sci.* **2012**, *5*, 6057−6060.

(5) Altinkaya, C.; Atli, A.; Atilgan, A.; Salimi, K.; Yildiz, A. Facile fabrication of low-cost low-temperature carbon-based counter electrode with an outstanding fill factor of 73% for dye-sensitized solar cells. *Int. J. Energy Res.* **2020**, *44*, 3160−3170.

(6) Chen, M.; Shao, L.-L. Review on the recent progress of carbon counter electrodes for dye-sensitized solar cells. *Chem. Eng. J.* **2016**, *304*, 629−645.

(7) Kumar, R.; More, V.; Mohanty, S. P.; Nemala, S. S.; Mallick, S.; Bhargava, P. A simple route to making counter electrode for dye sensitized solar cells (DSSCs) using sucrose as carbon precursor. *J. Colloid Interface Sci.* **2015**, *459*, 146−150.

(8) Kumar, R.; Nemala, S. S.; Mallick, S.; Bhargava, P. Synthesis and characterization of carbon based counter electrode for dye sensitized solar cells (DSSCs) using sugar free as a carbon material. *Sol. Energy* **2017**, *144*, 215−220.

(9) Kumar, R.; Bhargava, P. Fabrication of a counter electrode using glucose as carbon material for dye sensitized solar cells. *Mater. Sci. Semicond. Process.* **2015**, *40*, 331−336.

(10) Kumar, R.; Sahajwalla, V.; Bhargava, P. Fabrication of a counter electrode for dye-sensitized solar cells (DSSCs) using a carbon material produced with the organic ligand 2-methyl-8-hydroxyquinolinol (Mq). *Nanoscale Adv.* **2019**, *1*, 3192−3199.

(11) Kumar, R.; Bhargava, P. Synthesis and characterization of carbon based counter electrode for dye sensitized solar cells (DSSCs) using organic precursor 2-2′Bipyridine (Bpy) as a carbon material. *J. Alloys Compd.* **2018**, *748*, 905−910.

(12) Wu, J.; Lan, Z.; Lin, J.; Huang, M.; Huang, Y.; Fan, L.; Luo, G.; Lin, Y.; Xie, Y.; Wei, Y. Counter electrodes in dye-sensitized solar cells. *Chem. Soc. Rev.* **2017**, *46*, 5975−6023.

(13) Sarkar, A.; Bera, S.; Chakraborty, A. K. CoNi₂S₄-reduced graphene oxide nanohybrid: An excellent counter electrode for Pt-free DSSC. *Sol. Energy* **2020**, *208*, 139−149.

(14) Baptayev, B.; Mustazheb, D.; Abilova, Z.; Balanay, M. P. Nanostructured flower-shaped CuCo₂S₄ as a Pt-free counter-electrode for dye-sensitized solar cells. *Chem. Commun.* **2020**, *56*, 12190−12193.

(15) Ahmed, U.; Alizadeh, M.; Rahim, N. A.; Shahabuddin, S.; Ahmed, M. S.; Pandey, A. K. A comprehensive review on counter electrodes for dye sensitized solar cells: A special focus on Pt-TCO free counter electrodes. *Sol. Energy* **2018**, *174*, 1097−1125.

(16) Li, G. R.; Gao, X. P. Low-Cost Counter-Electrode Materials for Dye-Sensitized and Perovskite Solar Cells. *Adv. Mater.* **2020**, *32*, 1806478.

(17) Gao, C.; Han, Q.; Wu, M. Review on transition metal compounds based counter electrode for dye-sensitized solar cells. *J. Energy Chem.* **2018**, *27*, 703−712.

(18) Wu, M.; Ma, T. Recent progress of counter electrode catalysts in dye-sensitized solar cells. *J. Phys. Chem. C* **2014**, *118*, 16727−16742.

(19) Chen, M.; Shao, L.-L.; Yuan, Z.-Y.; Jing, Q.-S.; Huang, K.-J.; Huang, Z.-Y.; Zhao, X.-H.; Zou, G.-D. General strategy for controlled synthesis of NiₓPᵧ/carbon and its evaluation as a counter electrode material in dye-sensitized solar cells. *ACS Appl. Mater. Interfaces* **2017**, *9*, 17949−17960.

(20) Wang, S.; Xie, Y.; Shi, K.; Zhou, W.; Xing, Z.; Pan, K.; Cabot, A. Monodispersed nickel phosphide nanocrystals in situ grown on reduced graphene oxide with controllable size and composition as a counter electrode for dye-sensitized solar cells. *ACS Sustainable Chem. Eng.* **2020**, *8*, 5920−5926.

(21) Wu, M.; Bai, J.; Wang, Y.; Wang, A.; Lin, X.; Wang, L.; Shen, Y.; Wang, Z.; Hagfeldt, A.; Ma, T. High-performance phosphide/carbon counter electrode for both iodide and organic redox couples in dye-sensitized solar cells. *J. Mater. Chem.* **2012**, *22*, 11121−11127.

(22) Chen, M.; Shao, L.-L.; Dong, M.-Y.; Lv, X.-W.; Yuan, Z.-Y.; Qian, X.; Han, Y.-Y.; Ding, A.-X. Molecular-level synthesis of cobalt phosphide nanocrystals confined in highly nitrogen-doped mesoporous carbon electrocatalyst for highly efficient dye-sensitized solar cells. *ACS Sustainable Chem. Eng.* **2020**, *8*, 17245−17261.

(23) Shi, Z.; Feng, W.; Wang, X.; Li, M.; Song, C.; Chen, L. Catalytic cobalt phosphide Co₂P/carbon nanotube nanocomposite as host material for high performance lithium-sulfur battery cathode. *J. Alloys Compd.* **2021**, *851*, 156289.

(24) Wu, L.; Yu, L.; Zhang, F.; McElhenny, B.; Luo, D.; Karim, A.; Chen, S.; Ren, Z. Heterogeneous bimetallic phosphide Ni₂P-Fe₂P as an efficient bifunctional catalyst for water/seawater splitting. *Adv. Funct. Mater.* **2021**, *31*, 2006484.

(25) Chouki, T.; Machreki, M.; Emin, S. Solvothermal synthesis of iron phosphides and their application for efficient electrocatalytic hydrogen evolution. *Int. J. Hydrogen Energy* **2020**, *45*, 21473−21482.

(26) Li, S.; Wang, R.; Yang, X.; Wu, J.; Meng, H.; Xu, H.; Ren, Z. Binary metal phosphides with MoP and FeP embedded in P,N-doped graphitic carbon as electrocatalysts for oxygen reduction. *ACS Sustainable Chem. Eng.* **2019**, *7*, 11872−11884.

(27) Liu, M.; Li, J. Cobalt phosphide hollow polyhedron as efficient bifunctional electrocatalysts for the evolution reaction of hydrogen and oxygen. *ACS Appl. Mater. Interfaces* **2016**, *8*, 2158−2165.

(28) Peroni, M.; Lee, I.; Huang, X.; Baráth, E.; Gutiérrez, O. Y.; Lercher, J. A. Deoxygenation of palmitic acid on unsupported transition-metal phosphides. *ACS Catal.* **2017**, *7*, 6331−6341.

(29) Lutterotti, L. Total pattern fitting for the combined size-strain-stress-texture determination in thin film diffraction. *Nucl. Instrum. Methods Phys. Res., Sect. B* **2010**, *268*, 334−340.

(30) Atli, A.; Sutcu, I.; Kerem Yildiz, Z.; Yildiz, A. Optimizing deposition parameters of DSSCs composed of blue TiO₂. *IEEE J. Photovoltaics* **2021**, *11*, 118−123.

(31) Kresse, G.; Furthmüller, J. Efficient iterative schemes forab initiototal-energy calculations using a plane-wave basis set. *Phys. Rev. B: Condens. Matter Mater. Phys.* **1996**, *54*, 11169−11186.

(32) Perdew, J. P.; Burke, K.; Ernzerhof, M. Generalized gradient approximation made simple. *Phys. Rev. Lett.* **1996**, *77*, 3865−3868.

(33) Blöchl, P. E. Projector augmented-wave method. *Phys. Rev. B: Condens. Matter Mater. Phys.* **1994**, *50*, 17953.

(34) Monkhorst, H. J.; Pack, J. D. Special points for brillouin-zone integrations. *Phys. Rev. B: Solid State* **1976**, *13*, 5188−5192.

(35) Makov, G.; Payne, M. C. Periodic boundary conditions inab initiocalculations. *Phys. Rev. B: Condens. Matter Mater. Phys.* **1995**, *51*, 4014−4022.

(36) Park, J.; Koo, B.; Hwang, Y.; Bae, C.; An, K.; Park, J.-G.; Park, H. M.; Hyeon, T. Novel synthesis of magnetic Fe₂P nanorods from thermal decomposition of continuously delivered precursors using a syringe pump. *Angew. Chem., Int. Ed.* **2004**, *43*, 2282−2285.

(37) Rasras, A.; Hamdi, R.; Mansour, S.; Samara, A.; Haik, Y. Study of the magnetocaloric effect in single-phase antiferromagnetic GdMnO₃. *J. Phys. Chem. Solids* **2021**, *149*, 109798.

(38) Rghu, M. S.; Kumar, K. Y.; Prashanth, M. K.; Prasanna, B. P.; Vinuth, R.; Kumar, CB. P. Adsorption and antimicrobial studies of chemically bonded magnetic graphene oxide-Fe₃O₄ nanocomposite for water purification. *J. Water Process. Eng.* **2017**, *17*, 22−31.

(39) Vereshchagin, O. S.; Pankin, D. V.; Smirnov, M. B.; Vlasenko, N. S.; Shilovskikh, V. V.; Britvin, S. N. Raman spectroscopy: A promising tool for the characterization of transition metal phosphides. *J. Alloys Compd.* **2021**, *853*, 156468.

(40) Litasov, K. D.; Bekker, T. B.; Sagatov, N. E.; Gavryushkin, P. N.; Krinitsyn, P. G.; Kuper, K. E. (Fe,Ni)2P allabogdanite can be an ambient pressure phase in iron meteorites. *Sci. Rep.* **2020**, *10*, 8956.

(41) Yoon, C. H.; Vittal, R.; Lee, J.; Chae, W.-S.; Kim, K.-J. Enhanced performance of a dye-sensitized solar cell with an electrodeposited-platinum counter electrode. *Electrochim. Acta* **2008**, *53*, 2890−2896.

(42) Sing, K. The use of nitrogen adsorption for the characterisation of porous materials. *Colloids Surf., A* **2001**, *187−188*, 3−9.

(43) Patil, S. A.; Hussain, S.; Shrestha, N. K.; Mengal, N.; Jalalah, M.; Jung, J.; Park, J.-G.; Choi, H.; Kim, H.-S.; Noh, Y.-Y. Facile synthesis of cobalt-nickel sulfide thin film as a promising counter electrode for triiodide reduction in dye-sensitized solar cells. *Energy* **2020**, *202*, 117730.

(44) Murugadoss, V.; Arunachalam, S.; Elayappan, V.; Angaiah, S. Development of electrospun PAN/CoS nanocomposite membrane electrolyte for high-performance DSSC. *Ionics* **2018**, *24*, 4071−4080.

(45) Yue, G.; Li, F.; Tan, F.; Li, G.; Chen, C.; Wu, J. Nickel sulfide films with significantly enhanced electrochemical performance induced by self-assembly of 4-aminothiophenol and their application in dye-sensitized solar cells. *RSC Adv.* **2014**, *4*, 64068−64074.

(46) Vikraman, D.; Arbab, A. A.; Hussain, S.; Shrestha, N. K.; Jeong, S. H.; Jung, J.; Patil, S. A.; Kim, H.-S. Design of WSe₂/MoS₂ heterostructures as the counter electrode to replace Pt for dye-sensitized solar cell. *ACS Sustainable Chem. Eng.* **2019**, *7*, 13195−13205.

(47) Krishnapriya, R.; Nizamudeen, C.; Saini, B.; Mozumder, M. S.; Sharma, R. K.; Mourad, A. I. MOF-derived Co²⁺-doped TiO₂ nanoparticles as photoanodes for dye-sensitized solar cells. *Sci. Rep.* **2021**, *11*, 16265.

(48) Yin, Y.; Zhai, K.; Zhang, B.; Zhai, S. Electrical Resistivity of Iron Phosphides at High-Pressure and High-Temperature Conditions

With Implications for Lunar Core's Thermal Conductivity. *J. Geophys. Res.: Solid Earth* **2019**, *124*, 5544−5556.

(49) Tsai, C.-H.; Hsu, S.-Y.; Lu, C.-Y.; Tsai, Y.-T.; Huang, T.-W.; Chen, Y.-F.; Jhang, Y.-H.; Wu, C.-C. Influences of textures in Pt counter electrode on characteristics of dye-sensitized solar cells. *Org. Electron.* **2012**, *13*, 199−205.

(50) Yun, S.; Lund, P. D.; Hinsch, A. Stability assessment of alternative platinum free counter electrodes for dye-sensitized solar cells. *Energy Environ. Sci.* **2015**, *8*, 3495−3514.